the linearized matrix equation regarding the contact boundary conditions is expressed as:

$$\begin{bmatrix} [K^{\mathrm{m}}_{\Gamma,U}] & 0 & [K^{\mathrm{m}}_{\Gamma,\Lambda}] \\ 0 & [K^{\mathrm{s}}_{\Gamma,U}] & [K^{\mathrm{s}}_{\Gamma,\Lambda}] \\ [K^{\mathrm{m}}_{\Lambda,\Gamma}] & 0 & 0 \end{bmatrix} \begin{Bmatrix} \Delta\Gamma^{\mathrm{m}} \\ \Delta\Gamma^{\mathrm{s}} \\ \Delta\Lambda \end{Bmatrix} = \begin{Bmatrix} \Delta F^{\mathrm{m}}_{\Gamma} \\ \Delta F^{\mathrm{s}}_{\Gamma} \\ \Delta G_{\Lambda} \end{Bmatrix} \tag{A16}$$

It is noted that the resulting contact stiffness is an asymmetric matrix.

ACKNOWLEDGEMENTS

This work was supported by the Japan Society for the Promotion of Science through a Grant-in-Aid for Scientific Research (C) 14550067.

REFERENCES

1. Maroudas A. In *Physico-Chemical Properties of Articular Cartilage: Adult Articular Cartilage*, Freeman MAR (ed.). Pitman Medical: London, 1979.
2. Eisenberg SR, Grodzinsky AJ. The kinetics of chemically-induced nonequilibrium swelling of articular-cartilage and corneal stroma. *Journal of Biomechanical Engineering—Transactions of the ASME* 1987; **109**(1):79–89.
3. Frank EH, Grodzinsky AJ. Cartilage electromechanics. 1. Electrokinetic transduction and the effects of electrolyte Ph and ionic-strength. *Journal of Biomechanics* 1987; **20**(6):615–627.
4. Lanir Y. Biorheology and fluid flux in swelling tissues. 1. Bicomponent theory for small deformations, including concentration effects. *Biorheology* 1987; **24**(2):173–187.
5. Maroudas A, Bannon C. Measurement of swelling pressure in cartilage and comparison with the osmotic-pressure of constituent proteoglycans. *Biorheology* 1981; **18**(3–6):619–632.
6. Myers ER, Lai WM, Mow VC. A continuum theory and an experiment for the ion-induced swelling behavior of articular-cartilage. *Journal of Biomechanical Engineering—Transactions of the ASME* 1984; **106**(2):151–158.
7. Parsons JR, Black J. Mechanical-behavior of articular-cartilage—quantitative changes with alteration of ionic environment. *Journal of Biomechanics* 1979; **12**(10):765–773.
8. Frank EH, Grodzinsky AJ. Cartilage electromechanics. 2. A continuum model of cartilage electrokinetics and correlation with experiments. *Journal of Biomechanics* 1987; **20**(6):629–639.
9. Lai WM, Hou JS, Mow VC. A triphasic theory for the swelling and deformation behaviors of articular-cartilage. *Journal of Biomechanical Engineering—Transactions of the ASME* 1991; **113**(3):245–258.
10. Huyghe JM, Janssen JD. Quadriphasic mechanics of swelling incompressible porous media. *International Journal of Engineering Science* 1997; **35**(8):793–802.
11. Gu WY, Lai WM, Mow VC. A mixture theory for charged-hydrated soft tissues containing multi-electrolytes: passive transport and swelling behaviors. *Journal of Biomechanical Engineering—Transactions of the ASME* 1998; **120**(2):169–180.
12. Chen Y, Chen X, Hisada T. Non-linear finite element analysis of mechanical electrochemical phenomena in hydrated soft tissues based on triphasic theory. *International Journal for Numerical Methods in Engineering* 2006; **65**(2):147–173.
13. Sun DN, Gu WY, Guo XE, Lai WM, Mow VC. A mixed finite element formulation of triphasic mechano-electrochemical theory for charged, hydrated biological soft tissues. *International Journal for Numerical Methods in Engineering* 1999; **45**(10):1375–1402.
14. van Loon R, Huyghe JM, Wijlaars MW, Baaijens FPT. 3D FE implementation of an incompressible quadriphasic mixture model. *International Journal for Numerical Methods in Engineering* 2003; **57**(9):1243–1258.
15. Ateshian GA. A theoretical formulation for boundary friction in articular cartilage. *Journal of Biomechanical Engineering—Transactions of the ASME* 1997; **119**(1):81–86.
16. Ateshian GA, Lai WM, Zhu WB, Mow VC. An asymptotic solution for the contact of 2 biphasic cartilage layers. *Journal of Biomechanics* 1994; **27**(11):1347–1360.



DOI: 10.1002/nme

17. Ateshian GA, Wang H. A theoretical solution for the frictionless rolling contact of cylindrical biphasic articular cartilage layers—reply. *Journal of Biomechanics* 1997; **30**(1):99–99.
18. Ateshian GA, Wang HQ. A theoretical solution for the frictionless rolling-contact of cylindrical biphasic articular-cartilage layers. *Journal of Biomechanics* 1995; **28**(11):1341–1355.
19. Ateshian GA, Wang HQ, Lai WM. The role of interstitial fluid pressurization and surface porosities on the boundary friction of articular cartilage. *Journal of Tribology—Transactions of the ASME* 1998; **120**(2):241–248.
20. Federico S, La Rosa G, Herzog W, Wu JZ. Effect of fluid boundary conditions on joint contact mechanics and applications to the modeling of osteoarthritic joints. *Journal of Biomechanical Engineering—Transactions of the ASME* 2004; **126**(2):220–225.
21. Hlavacek M. A note on an asymptotic solution for the contact of two biphasic cartilage layers in a loaded synovial joint at rest. *Journal of Biomechanics* 1999; **32**(9):987–991.
22. Kelkar R, Ateshian GA. Contact creep of biphasic cartilage layers. *Journal of Applied Mechanics—Transactions of the ASME* 1999; **66**(1):137–145.
23. Wu JZ, Herzog W. On the pressure gradient boundary condition for the contact of two biphasic cartilage layers. *Journal of Biomechanics* 2000; **33**(10):1331–1332.
24. Wu JZ, Herzog W, Epstein M. An improved solution for the contact of two biphasic cartilage layers. *Journal of Biomechanics* 1997; **30**(4):371–375.
25. Wu JZ, Herzog W, Epstein M. Articular joint mechanics with biphasic cartilage layers under dynamic loading. *Journal of Biomechanical Engineering—Transactions of the ASME* 1998; **120**(1):77–84.
26. Wu JZ, Herzog W, Ronsky J. Modeling axi-symmetrical joint contact with biphasic cartilage layers—an asymptotic solution. *Journal of Biomechanics* 1996; **29**(10):1263–1281.
27. Donzelli PS, Spilker RL. A contact finite element formulation for biological soft hydrated tissues. *Computer Methods in Applied Mechanics and Engineering* 1998; **153**(1–2):63–79.
28. Donzelli PS, Spilker RL, Ateshian GA, Mow VC. Contact analysis of biphasic transversely isotropic cartilage layers and correlations with tissue failure. *Journal of Biomechanics* 1999; **32**(10):1037–1047.
29. Dunbar WL, Un K, Donzelli PS, Spilker RL. An evaluation of three-dimensional diarthrodial joint contact using penetration data and the finite element method. *Journal of Biomechanical Engineering—Transactions of the ASME* 2001; **123**(4):333–340.
30. Han SK, Federico S, Epstein M, Herzog W. An articular cartilage contact model based on real surface geometry. *Journal of Biomechanics* 2005; **38**(1):179–184.
31. Krishnan R, Park S, Eckstein F, Ateshian GA. Inhomogeneous cartilage properties enhance superficial interstitial fluid support and frictional properties, but do not provide a homogeneous state of stress. *Journal of Biomechanical Engineering—Transactions of the ASME* 2003; **125**(5):569–577.
32. Wu JZ, Herzog W, Epstein M. Evaluation of the finite element software ABAQUS for biomechanical modelling of biphasic tissues. *Journal of Biomechanics* 1998; **31**(2):165–169.
33. Yang T, Spilker RL. A Lagrange multiplier mixed finite element formulation for three-dimensional contact of biphasic tissues. *Journal of Biomechanical Engineering—Transactions of the ASME* 2007; **129**(3):457–471.
34. Pawaskar SS, Jin ZM, Fisher J. Modelling of fluid support inside articular cartilage during sliding. *Proceedings of the Institution of Mechanical Engineers Part J-Journal of Engineering Tribology* 2007; **221**(J3):165–174.
35. Chen X, Chen Y, Hisada T. Development of a finite element procedure of contact analysis for articular cartilage with large deformation based on the biphasic theory. *JSME International Journal Series C-Mechanical Systems Machine Elements and Manufacturing* 2005; **48**(4):537–546.
36. Setton LA, Tohyama H, Mow VC. Swelling and curling behaviors of articular cartilage. *Journal of Biomechanical Engineering—Transactions of the ASME* 1998; **120**(3):355–361.
37. Bachrach NM, Valhmu WB, Stazzone E, Ratcliffe A, Lai WM, Mow VC. Changes in proteoglycan synthesis of chondrocytes in articular cartilage are associated with the time-dependent changes in their mechanical environment. *Journal of Biomechanics* 1995; **28**(12):1561–1569.
38. Huyghe JM, Janssen CF, van Donkelaar CC, Lanir Y. Measuring principles of frictional coefficients in cartilaginous tissues and its substitutes. *Biorheology* 2002; **39**(1–2):47–53.
39. Ateshian GA, Soltz MA, Mauck RL, Basalo IM, Hung CT, Lai WM. The role of osmotic pressure and tension-compression nonlinearity in the frictional response of articular cartilage. *Transport in Porous Media* 2003; **50**(1–2):5–33.
40. Hou JS, Holmes MH, Lai WM, Mow VC. Boundary-conditions at the cartilage–synovial fluid interface for joint lubrication and theoretical verifications. *Journal of Biomechanical Engineering—Transactions of the ASME* 1989; **111**(1):78–87.



DOI: 10.1002/nme

41. El-Abbasi N, Bathe KJ. Stability and patch test performance of contact discretizations and a new solution algorithm. *Computers and Structures* 2001; **79**(16):1473–1486.
42. Chen X, Hisada T. Development of a finite element contact analysis algorithm to pass the patch test. *JSME International Journal Series A—Solid Mechanics and Material Engineering* 2006; **49**(4):483–491.
43. Mow VC, Ateshian GA, Lai WM, Gu WY. Effects of fixed charges on the stress-relaxation behavior of hydrated soft tissues in a confined compression problem. *International Journal of Solids and Structures* 1998; **35**(34–35):4945–4962.



DOI: 10.1002/nme

# The sinus of Valsalva relieves abnormal stress on aortic valve leaflets by facilitating smooth closure

Susumu Katayama, BE, Nobuyuki Umetani, BE, Seiryo Sugiura, MD, PhD, and Toshiaki Hisada, PhD

**Objective:** Recently, various modifications have been made to aortic root replacement procedures to include the pseudosinus in the synthetic graft, but its effect on valve function still remains to be elucidated. The purpose of this study was to compare the flow dynamics and its influence on the stress/strain in the valve leaflet in two types of aortic root, either with or without the pseudosinus, with a simulation model.

**Methods:** The proximal portions of the ascending aorta and aortic valves were modeled with blood flowing inside. Blood flow and the motion of aortic valve leaflets were studied while applying a physiologic pressure waveform using fluid–structure interaction finite element analysis. Waveforms were varied to simulate the change in cardiac contractility.

**Results:** In the aorta without the sinus, the time during which the valve was open was longer and the rapid valve closing velocity was faster under all conditions studied. In the pseudosinus model, we could clearly observe vortex formation from the early phase of ejection, which seemed to facilitate the gradual but smooth closure of the valve. Valve leaflets without the sinus were subject to greater stress and underwent bending deformation in the longitudinal direction.

**Conclusions:** Sinuses of Valsalva facilitate the smooth closure of the aortic valve, thereby avoiding the building up of abnormal stress in the leaflet. Such an effect may assure the durability of valve leaflets in aortic grafts with a pseudosinus.


Video clip is available online.

Supplemental material is available online.

Sinuses of Valsalva, with their characteristic morphologic features, have attracted the interest of researchers, and earlier modeling studies have suggested that the sinuses function not only to prevent the contact of valve leaflet with the aortic wall, but also to facilitate valve closure by the formation of vortices inside them.[1,2] The emergence of valve-sparing aortic root replacement procedures for the treatment of patients with aortic root disease has provided us with the unique opportunity to test such hypotheses. Leyh and colleagues[3] compared patients who had undergone tube replacement of the aortic root (reimplantation [David I] procedure) and those who had undergone separate replacement of the sinuses of Valsalva (remodeling [Yacoub] procedure) to find that the near-normal opening and closing characteristics of valves were achieved by the preservation of the shape and independent mobility of the sinuses. On the other hand, de Oliveira and associates,[4] based on a decade of following up surgically treated patients, reported a reduced risk of postoperative aortic insufficiency in patients with reimplantation. They concluded that the implantation procedure secures the entire aortic valve inside the Dacron graft to prevent dilatation of the aortic root and concomitant regurgitation. However, they also recognized the elimination of sinuses as a shortcoming of their technique, and they, as well as other surgeons, have modified their reimplantation techniques to create graft pseudosinuses.[5-7]

Although it is generally assumed that smooth opening and closing relieved the abnormal stress and strain on leaflets, neither clinical observations[3,8-10] nor experimental studies using a mock circulation[11,12] could provide us with detailed information on the stress and/or strain distribution in the leaflet to clarify this assumption. An alternative approach to overcome such technical difficulty and obtain stress and strain distribution is a simulation study using finite element analysis. Grande-Allen and associates[13] created finite element models of the aortic root and valve with a cylindrical graft, a tailored graft sutured just above the valve, and a pseudosinus graft, to find that the cylindrical graft created the greatest stress. Beck, Thubrikar, and Robicsek[14] also compared the finite element models of the tubular aortic root and the root with sinuses under pressure to find that a stress concentration along the leaflet attachment develops only in

From the Department of Human and Engineered Environmental Studies, Graduate School of Frontier Sciences, The University of Tokyo, Kashiwa-shi, Chiba, Japan.
This study was supported by Core Research for Evolutional Science and Technology (CREST) program by Japan Science and Technology Agency (JST).
Received for publication Feb 25, 2008; revisions received April 22, 2008; accepted for publication May 19, 2008.
Address for reprints: Seiryo Sugiura, MD, PhD, Department of Human and Engineered Environmental Studies, Graduate School of Frontier Sciences, The University of Tokyo, 5-1-5 Kashiwa-no-ha, Kashiwa-shi, Chiba, Japan (E-mail: Sugiura@k.u-tokyo.ac.jp).
J Thorac Cardiovasc Surg 2008;136:1528-35
0022-5223/$34.00

doi:10.1016/j.jtcvs.2008.05.054

**Abbreviations and Acronyms**

ALE = arbitrary Lagrangian–Eulerian
C = cylindrical graft
DOF = degree of freedom
P = pseudosinus graft
P90 = peak pressure of 90%
P100 = control peak pressure
P110 = peak pressure of 110%
RVCV = rapid valve closing velocity
SCD = slow closing distance

the tubular root. Although these studies gave strong support to surgeons' beliefs, the simulation was done only by applying pressure to the model, thus totally ignoring the influence of the blood flow, which most of the surgeons and researchers are interested in. The capabilities of the fluid–structure interaction finite element method for the analysis of the aortic valve were first shown by Nicosia and colleagues[15] using a commercial software package; subsequently, de Hart and coworkers[16] analyzed the normal aortic root using the fictitious domain method. However, owing to the numerical instability of the method, an unphysiologically low Reynolds number flow was introduced.

We[17] have developed a numerical approach for fluid–structure interaction analysis based on the arbitrary Lagrangian–Eulerian (ALE) finite element method and applied it to the multiphysics simulation of the heart.[18-21] In this study, we applied this method to the analysis of the dynamics of aortic valve opening and closure in two different models of the aortic root, with or without the sinuses of Valsalva. It will be clearly shown that the sinuses, by promoting vortex formation, facilitate the smooth closure of the aortic valve and circumvent the development of abnormal stress in the leaflets.

## METHOD

### Modeling the Aortic Root

We created the shapes of cylindrical graft and pseudosinus graft with the dimensions shown in Figure 1, *A*. Then, we modeled the blood domain by tetrahedral finite elements with four velocity nodes and four pressure nodes, resulting in the total numbers of elements and the degree of freedom (DOF) of 4408 (24990 DOF) for the cylindrical model and 52620 (30658 DOF) for the pseudosinus model. For the valve leaflets, we adopted discrete Kirchhoff triangular shell elements with anisotropic material property originating from the fiber orientation[15,22] (Figure 1, *B*). Furthermore, the edge of each leaflet was made thicker according to the literature.[23] For the material properties of the valve, see Table E1.

### The Heart and the Systemic Circulation as Boundary Conditions

To the distal end of the models, we connected the 3-element Windkessel model of systemic circulation. Pumping function of the heart was simulated by applying the physiologic pressure wave (minimum 75 mm Hg, maximum 120 mm Hg). To simulate cases in which contractility of the heart is either depressed (heart failure) or augmented, we varied the peak pressure to 90% (P90) or 110% (P110) of the control (P100) condition while keeping the pressure time products constant (Figure 1, *C*). This was intended because we usually observed a slowed time course of contraction when the contractility was depressed.

### Computation

We used a strongly coupled fluid–structure interaction finite element analysis program, which we have developed[17] and applied to various problems such as pulsation of the heart.[18-21] In this program, the Navier–Stokes equation is described in ALE coordinates, which artificially deform and move according to the instantaneous deformation of the fluid–structure interface. Furthermore, the fluid meshes and structure meshes are generated to coincide with each other on the interface at the beginning of the analysis. Therefore, the geometric compatibility and balance of traction forces are automatically satisfied by merging both meshes on the interface. The disadvantage of the method is the distortion of ALE meshes. Because the fluid–structure interface moves largely in the case of a heart valve problem, excessive ALE mesh distortion occurs, resulting in the degradation of element performance. To avoid such a problem, we applied an automatic mesh reconnecting algorithm, which our group has developed. All of the program codes were written in the laboratory.

## RESULTS

The flow dynamics and the motion of the valves in cylindrical and pseudosinus grafts can be seen in the online supplementary Movies E1 and E2. In the pseudosinus graft, we can clearly observe the formation of vortices of counterclockwise rotation in the sinuses, which seems to facilitate the closure by pushing the leaflets. In the cylindrical graft, the edges of the leaflets make contact with the wall when they are fully open and the closure seemed to be retarded. Peak velocity values were 0.95 m/s (P90), 1.04 m/s (P100), and 1.16 m/s (P110) and the corresponding Reynolds numbers were 2995, 3278, and 3657, respectively.

### Motion of the Leaflets

To quantify the motion of the leaflets and compare the simulation results with clinical observations, we traced the edge of the leaflet and plotted the distance from the axis of the aorta as a function of time, as we do in M-mode echocardiography (Figure 2, *A*), and calculated the slow closing distance (SCD = [D1 − D2]/D1) and closing time (Figure 2, *B*). SCD values were greater for pseudosinus models (P) than for cylindrical models (C) under all of the conditions studied, but the difference was pronounced in response to low ejecting pressure (P vs C [%]: 8.9 vs, 5.1 [P110], 7.7 vs 4.6 [P100], and 6.3 vs 0.6 [P90]) (Figure 3, *A*). On the contrary, although the differences were small, closing time tended to be longer with the cylindrical model (P vs C [s]: 0.22 vs 0.24 [P110], 0.24 vs 0.25 [P100], and 0.26 vs 0.28 [P90]) (Figure 3, *B*). We also calculated the rapid valve closing velocity (RVCV) as the ratio between D2 and rapid closing time (*RCT* in Figure 2, *B*). RVCV was also faster for cylindrical models (P vs C [cm/s]: 50.6 vs 52.1 [P110], 49.8 vs 58.5 [P100], and 30.8 vs 42.7 [P90]) (Figure 3, *C*). These results can be taken to indicate that, in the presence

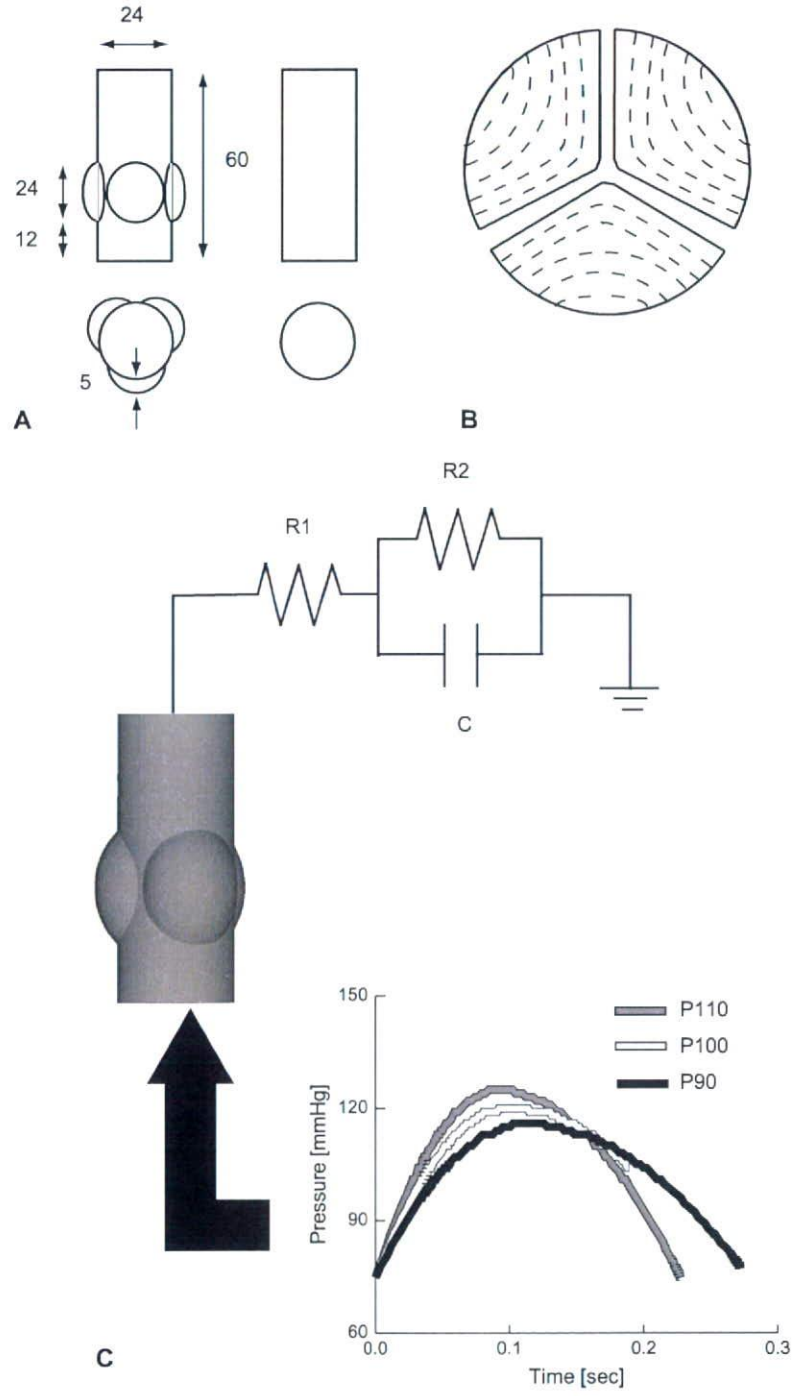


**FIGURE 1.** Configurations of the model. A, Cylindrical *(left)* and pseudosinus *(right)* aortic roots with details of their dimensions. B, Valvular leaflet and fiber orientation *(right)*. C, Simulated aortic pressure was applied to the proximal end of the model aortic root. To the distal end, a 3-element Windkessel model was connected. *R1*, Characteristic impedance (100 dynes · s · $cm^{-5}$); *R2*, peripheral resistance (1600 dynes · s · $cm^{-5}$); *C*, capacitance ($2.1 \times 10^{-3}$ L/mm Hg).

of pseudosinuses, the valvular leaflets initiate their motion from the earlier phase of ejection and gradually return to their closing positions. On the other hand, with the cylindrical model, valves are wide open until the late phase of ejection, during which the flow direction is reversed to increase the regurgitant fraction (P vs C [%]: 0.7 vs 4.4 [P110], 1.6 vs 4.2 [P100], and 0.4 vs 5.4 [P90]) (Figure 3, *D*).

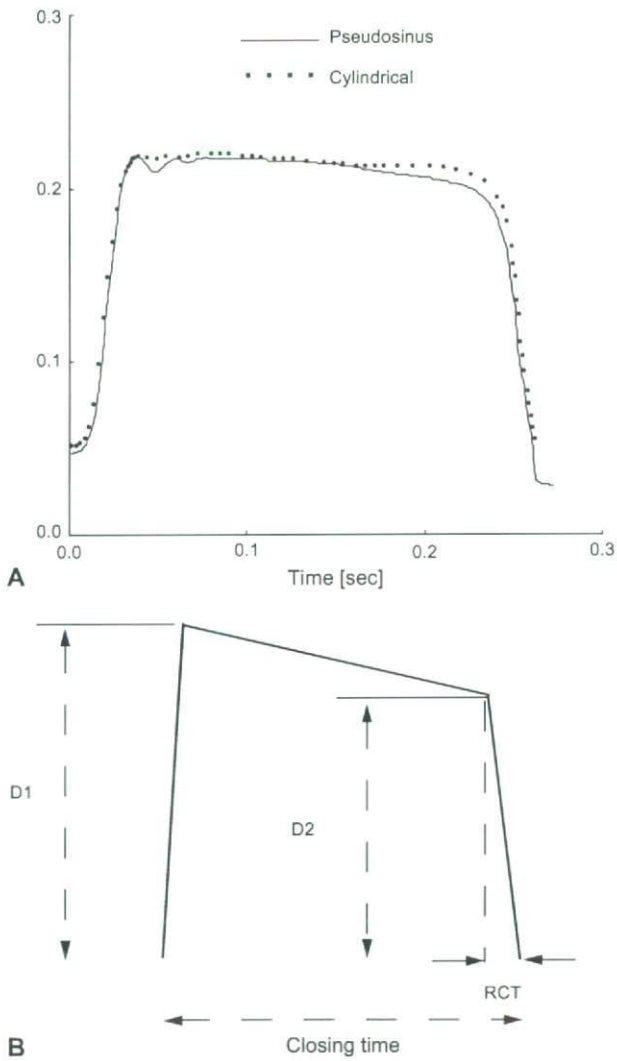


**FIGURE 2.** Motion of the leaflet. A, The distance from the axis of the aorta is shown as a function of time. *Solid line*, Pseudosinus model; *dotted line*, cylindrical model. B, Schematic diagram showing the indices characterizing the motion of leaflet. *D1*, Maximum distance; *D2*, distance immediately before the rapid closing. *RCT*, Rapid closing time.

### Strains and Stresses in the Leaflets

We also compared the strains and stresses in the leaflets between the two models. Taking into consideration the anisotropic material property reflecting the fiber orientation and the complex deformation each leaflet undergoes during the ejection, we calculated the peak stretch (membrane), bending, and total strains ($\epsilon$) parallel (||) and perpendicular (tt) to the fiber orientation. As shown in Figure 4, *A*, the leaflets in the cylindrical model experience greater peak strains, especially in the direction perpendicular to the fiber orientation (C vs P: 0.022 vs 0.012 [membrane$\epsilon$||], 0.042 vs 0.024 [membrane$\epsilon$tt], 0.069 vs 0.069 [bending$\epsilon$||], 0.087 vs 0.064 [bending$\epsilon$tt], 0.065 vs 0.060 [total$\epsilon$||], 0.089 vs 0.068 [total$\epsilon$tt]). Interestingly, the bending strains in the fiber direction did not differ appreciably between the two models. Comparison of peak stress ($\sigma$) values followed similar pattern to the strain values (C vs P [kPa]: 15.9 vs 8.6 [membrane$\sigma$||], 9.8 vs 5.6 [membrane$\sigma$tt], 48.0 vs 48.1 [bending$\sigma$||], 20.3 vs 14.8 [bending$\sigma$tt], 45.3 vs 41.8 [total$\sigma$||], 20.8 vs 15.7 [total$\sigma$tt]) (Figure 4, *B*).

## DISCUSSION

In this study, we applied the fluid–structure interaction finite element method to analyze the flow dynamics in the aortic root and the motion of the aortic valve. Comparison of two models with or without the sinuses of Valsalva clearly demonstrated their functional role in achieving the smooth closure of the valves. These results also have relevance to aortic root surgery, modifications to the procedures for which have been proposed to improve the prognoses of patients.

### Simulations of Aortic Root

Compared with studies using mock circulation,[1,11,12] simulation studies using the finite element method have advantages in that (1) the shape and the material properties of the model and experimental conditions can be altered and controlled over a wide range, (2) detailed data on the distribution of flow velocity and pressure are available, and (3) stress/strain distribution in the aortic wall and/or valvular leaflet can be calculated. In particular, stress data are important but hard to obtain in clinical settings.

However, so far, we can find only a few simulation studies in which fluid–structure interactions were analyzed, probably owing to the computational difficulties.[15,16,24] Among these studies, Nicosia and colleagues[15] constructed an anatomically accurate 3-dimensional finite element model in which both the aortic root and valves were represented by Hughes–Liu shell elements. They analyzed the blood flow and the motion of the valve leaflet during ejection by using LS-Dyna—an explicit finite element commercial code. Their pioneering work showed the potential capabilities of the fluid–structure finite element analysis for heart valve problems. However, some unphysiologic conditions, such as the 98.5% reduction in the bending stiffness of the valve leaflets, were introduced to reproduce their pliability, which in turn enforced the scaling down of the magnitude of the peak diastolic pressure to avoid valve element distortion. After Nicosia and colleagues,[15] de Hart and associates,[16] using the fictitious-domain method, successfully showed that vortex formation in the sinuses of Valsalva is essential for the smooth operation of the aortic valve. In contrast to the present study, however, their computation was carried out with an unphysiologically low Reynolds number (~900) owing to the numerical instabilities inherent in the algorithm.

Furthermore, a comparison of two clinically relevant models, namely, cylindrical and pseudosinus, based on fluid–structure interaction analysis, has been made for the

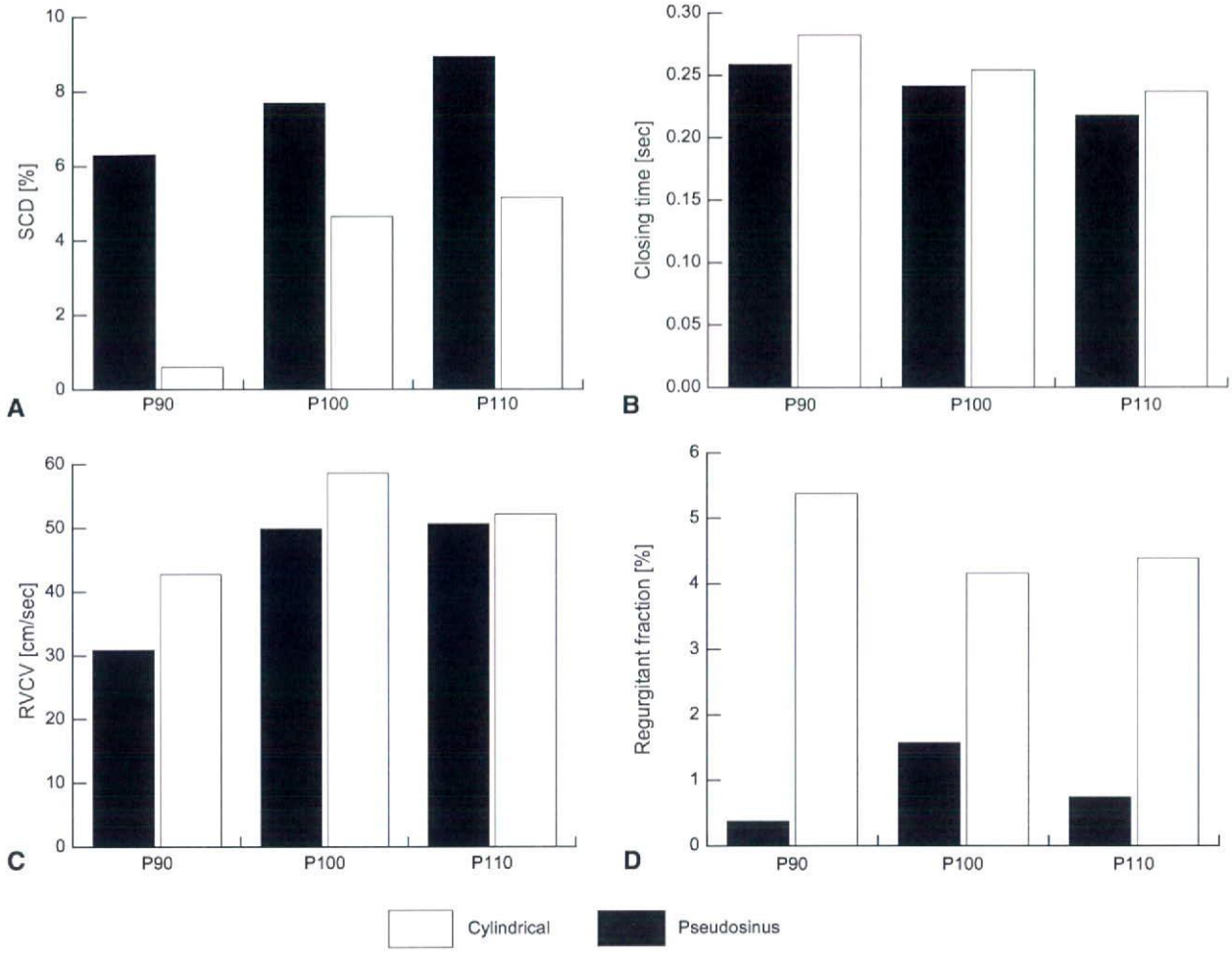


**FIGURE 3.** Comparison of valve functions. A, Slow closing distance *(SCD)*. B, Closing time. C, Rapid valve closing velocity *(RVCV)*. D, Regurgitant fraction. *White bar*, Cylindrical model; *black bar*, pseudosinus model.

first time. Although we can find the finite element analysis studies comparing the principal tensile stress of leaflets between the cylindrical graft and pseudosinus graft,[13,14] in those study, the calculation was carried out for only the diastolic period by applying the pressure, thus completely ignoring the influence of blood flow.

### Comparison With Experimental and Clinical Studies

Using the time-resolved 3-dimensional magnetic resonance velocity mapping, Markl and associates[10] compared vortex formation among patients who had undergone cylindrical graft (David I procedure) and those who had undergone neosinus graft (David V and David V-$S_{mod}$ [Stanford modification]), with normal volunteers as controls. Even though vorticity was increased in patients who underwent the David V procedure, because the difference did not reach statistical significance, they concluded that, although vortex formation was enhanced by the David V procedure, normal vorticity was preserved even without the sinus creation in the graft. Direct comparison with the current simulation results is difficult, because in this study a rigid tube with perfect cylindrical form was used, but a small degree of vortex formation was also identified in our simulation (Movie E2).

In a study comparing the motion of the leaflets between the patients who had undergone tube graft and those who had undergone remodeling (Yacoub) procedure, Leyh and coworkers[3] reported that, in patients who had undergone remodeling, SCD was greater but closing time was shorter, consistent with the present results. A similar tendency was reported for the comparison between patients with a tube graft and those with a newly developed graft with a pseudosinus.[8] However, the RVCV differed between the two studies. Leyh and coworkers[3] found that the RVCV was slower for tube grafts, but De Paulis and associates[8] reported results to the contrary.

In vitro studies may help to resolve this discrepancy. Fries and coworkers[11] placed a porcine aortic root operated on with either the David (cylinder) or Yacoub (remodeling) procedure

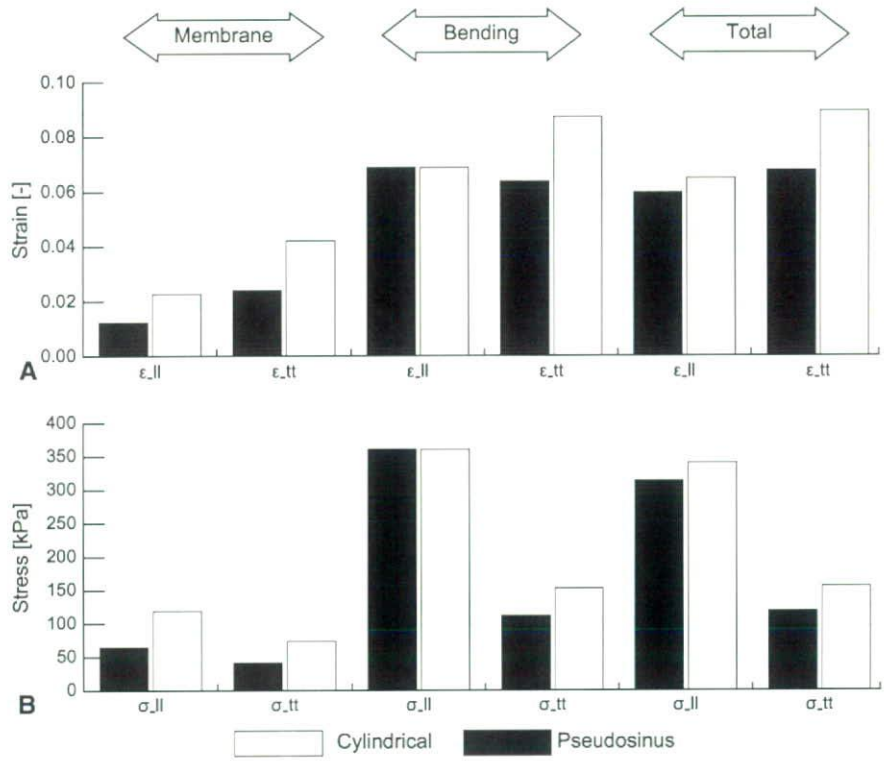


**FIGURE 4.** Strain and stress in the leaflet. A, Strain ($\epsilon$). B, Stress ($\sigma$). Values for membrane (tensile), bending, and total are shown in parallel (||) and perpendicular (tt) to the fiber direction. *White bar*, Cylindrical model; *black bar*, pseudosinus model.

in a mock circulation and recorded the motion of the valve. The difference in SCD was similar to the clinical observation mentioned above, as well as the present results, but they found that the differences in RVCV were dependent on cardiac output and that the RVCV was greater for the David procedure only at low cardiac output, similar to the present result (Figure 3, *C*). These contradictory results may have arisen because the patients in the study by Leyh and colleagues[3] had relatively high cardiac function (ejection fraction > 60%) compared with patients in other studies (about 50%).

As we mentioned earlier, the stresses and/or strains in the leaflet during ejection are hard to measure, but there has been a study in which strains were compared among the various surgical procedures.[12] From the images of porcine aortic roots operated on differently and placed in the mock circulation, the authors of this study calculated the cusp-bending deformation index in mid-systole as the fold depth normalized to the size of the leaflet. Although the index of strain used in this study was just an estimate, their results demonstrated a greater strain associated with the reimplantation procedure (tube graft), compatible with our simulation result.

### Implications

Although the creation of sinuses in remodeling procedures introduces the smooth closure of the aortic valve,[3] a long-term follow-up study demonstrated a better prognosis for patients undergoing the reimplantation (David I) procedure in terms of freedom from aortic regurgitation,[4] mainly because of the more reliable annular stabilization with this technique. However, the importance of the sinuses of Valsalva is widely recognized by cardiac surgeons, and various modifications to the reimplantation procedure have been proposed to achieve both annular stability and the creation of sinuses.[6-8,25,26] Although these techniques are expected to enhance the long-term durability of the leaflet, greater knowledge of the functional anatomy of the aortic root is required to achieve optimal results.[27] The current simulation would serve as a useful tool for designing tailor-made aortic grafts and, in fact, has provided us with new insight into the mechanics of the aortic valve leaflet during ejection.

Shown in Figure 5, *A*, are the stress distributions in the leaflets during the late phase of ejection for pseudosinus *(upper panel)* and cylindrical *(lower panel)* grafts (Movie E3). It can clearly be seen that the leaflet in the cylindrical graft is bent in its middle portion by being pushed by the retrograde flow from both sides (Movie E4). On the other hand, the leaflet in the pseudosinus graft has already returned halfway to the closed position, as evidenced by the large SCD, and accommodates the retrograde flow only on one side to avoid the abnormal bending stresses perpendicular to the fiber

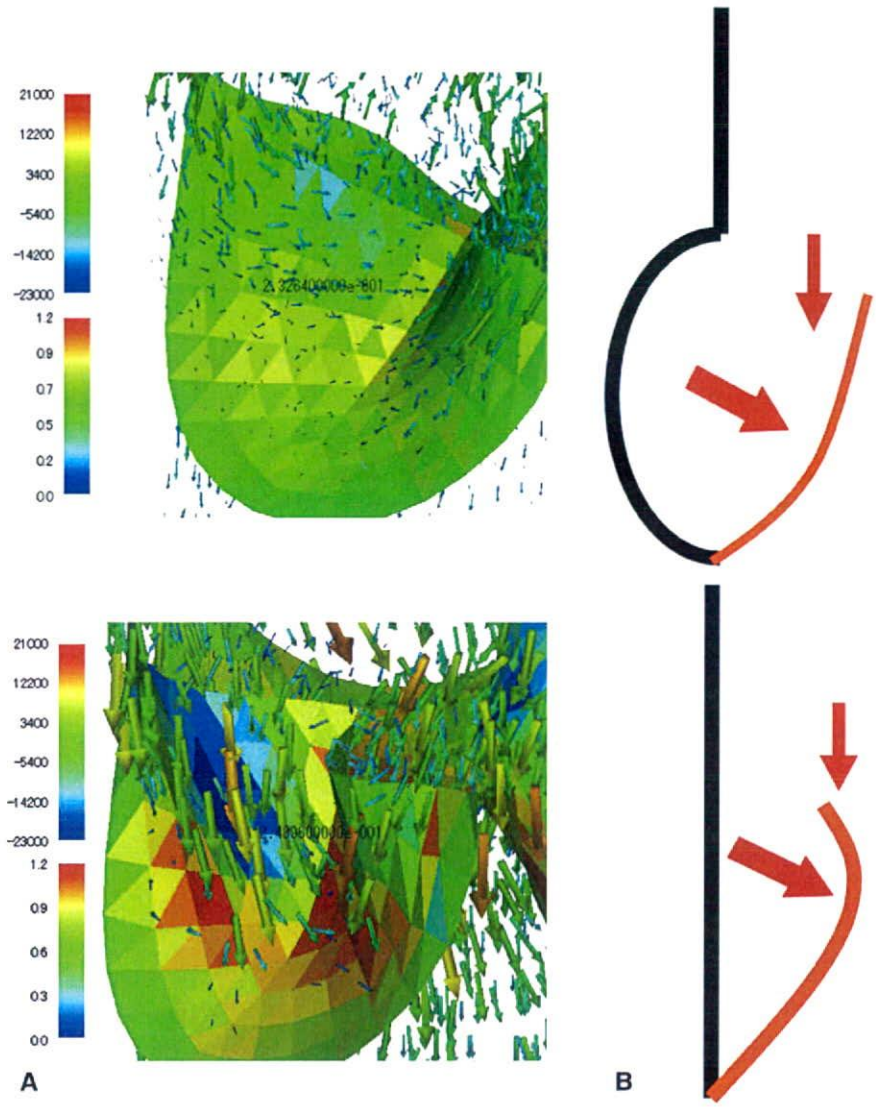


**FIGURE 5.** Stress in the leaflet and deformation. A, Close-up views of the leaflet in the late phase of ejection for pseudosinus *(upper panel)* and cylindrical *(lower panel)* models. Stress values shown in color coding indicate the higher stress in the cylindrical model. B, Schematic diagrams showing the direction of stress and induced deformation of the leaflets for pseudosinus *(upper panel)* and cylindrical *(lower panel)* models. Movies corresponding to this figure are available online.



orientation (Figure 5, *B*). So far, the stresses in the leaflet have been discussed mainly during diastole when leaflets are in the closed position, but the current simulation study demonstrated another important time point when abnormal stresses could build up, as well as the importance of fluid–structure interaction in consideration of designing the aortic root grafts.

### Limitation of the Study

In this simulation, only the short segment of ascending aorta was modeled as a rigid tube. Furthermore, applied pressure and systemic circulation approximated by the 3-element Windkessel model are simplifications of the real situation. These points should be improved to achieve more realistic and useful simulations. Use of clinical imaging data should also be considered. We are now working to model the entire thoracic aorta with realistic properties based on patients' computed tomographic data.

## CONCLUSION

Sinuses of Valsalva facilitate the smooth closure of the aortic valve, thereby avoiding the building up of abnormal stress in the leaflet. With further improvement in modeling, the fluid–structure interaction analysis of aortic root dynamics can be a powerful tool for the optimum design of aortic root surgery.

## References


1. van Steenhoven AA, van Dongen MEH. Model studies of the closing behavior of the aortic valve. *J Fluid Mech*. 1979;90:21-32.
2. Fung YC. How are the heart valves operated? Biomechanics, circulation. 2nd ed. New York: Springer-Verlag; 1997. p. 42-9.
3. Leyh RG, Schimidke C, Sievers H-H, Yacoub MH. Opening and closing characteristics of the aortic valve after different types of valve-preserving surgery. *Circulation*. 1999;100:2153-60.
4. de Oliveira NC, David TE, Ivanov J, Armstrong S, Eriksson MJ, Rakowski H, et al. Results of surgery for aortic root aneurysm in patients with Marfan syndrome. *J Thorac Cardiovasc Surg*. 2003;125:789-96.
5. David TE, Armstrong S, Ivanov J, Feindel CM, Omran A, Webb G. Results of aortic valve–sparing operations. *J Thorac Cardiovasc Surg*. 2001;122:39-46.
6. Demers P, Miller DC. Simple modification of "T. David-V" valve-sparing aortic root replacement to create graft pseudosinuses. *Ann Thorac Surg*. 2004;78:1479-81.
7. Takamoto S, Nawata K, Morota T. A simple modification of 'David-V' aortic root reimplantation. *Eur J Cardiothorac Surg*. 2006;30:560-2.
8. De Paulis R, De Matteis GM, Nardi P, Scaffe R, Buratta MM, Chiariello L. Opening and closing characteristics of the aortic valve after valve-sparing procedure using a new aortic root conduit. *Ann Thorac Surg*. 2001;72:487-94.
9. De Paulis R, De Matteis GM, Nardi P, Raffaele S, Bassano C, Chiariello L. Analysis of valve motion after reimplantation type of valve-sparing procedure (David I) with a new aortic root conduit. *Ann Thorac Surg*. 2002;74:53-7.
10. Markl M, Draney MT, Miller DC, Levin JM, Williamson EE, Pelc NJ, et al. TIme-resolving three-dimensional magnetic resonance velocity mapping of aortic flow in healthy volunteers and patients after valve-sparing aortic root replacement. *J Thorac Cardiovasc Surg*. 2005;130:456-63.
11. Fries R, Graeter T, Aicher D, Reul H, Schmitz C, Böhm M, et al. In vitro comparison of aortic valve movement after valve-preserving aortic replacement. *J Thorac Cardiovasc Surg*. 2006;132:32-7.
12. Erasmi A, Sievers H-H, Scharfschwerdt M, Eckel T, Misfeld M. In vitro hydrodynamics, cusp-bending deformation, and root distensibility for different types of aortic valve–sparing operations: remodeling, sinus prosthesis, and reimplantation. *J Thorac Cardiovas Surg*. 2005;130:1044-9.
13. Grande-Allen KJ, Cochran RP, Reinhall PG, Kunzelman KS. Re-creation of sinuses is important for sparing the aortic valve: a finite element study. *J Thorac Cardiovasc Surg*. 2000;119:753-63.
14. Beck A, Thubrikar MJ, Robicsek F. Stress analysis of the aortic valve with and without the sinuses of valsalva. *J Heart Valve Dis*. 2001;10:1-11.
15. Nicosia MA, Cochran RP, Einstein DR, Rutland CJ, Kunzelman KS. A coupled fluid–structure finite element model of the aortic valve root. *J Heart Valve Dis*. 2003;12:781-9.
16. De Hart J, Peters GW, Schreurs PJ, Baaijens FP. A three-dimensional computational analysis of fluid–structure interaction in the aortic valve. *J Biomech*. 2003;36:103-12.
17. Zhang Q, Hisada T. Analysis of fluid–structure interaction problems with structural buckling and large domain changes by ALE finite element method. *Comput Methods Appl Mech Engrg*. 2001;190:6341-57.
18. Watanabe H, Hisada T, Sugiura S, Okada J, Fukunari H. Computer simulation of blood flow, left ventricular wall motion and their interrelationship by fluid–structure interaction finite element method. *JSME Internatl J C*. 2002;45:1003-12.
19. Watanabe H, Sugiura S, Hisada T. Finite element analysis on the relationship between left ventricular pump function and fiber structure within the wall. *JSME Internatl J C*. 2003;46:1330-9.
20. Watanabe H, Sugano T, Sugiura S, Hisada T. Finite element analysis of ventricular wall motion and intra-ventricular blood flow in heart with myocardial infarction. *JSME Internatl J C*. 2004;47:1019-26.
21. Watanabe H, Sugiura S, Hisada T. Multi-physics simulation of left ventricular filling dynamics using fluid–structure interaction finite element method. *Biophys J*. 2004;87:2074-85.
22. Swanson WM, Clark RE. Dimensions and geometric relationship of the human aortic valve as a function of pressure. *Circ Res*. 1974;35:871-82.
23. Sahasakul Y, Edwards WD, Naessens JM, Tajik AJ. Age-related changes in aortic and mitral valve thickness: implications for two-dimensional echocardiography based on an autopsy study of 200 normal human hearts. *Am J Cardiol*. 1988; 62:424-30.
24. Peskin CS, McQueen DM. A three-dimensional computational model for blood flow in the heart: I. Immersed elastic fibers in a viscous incompressible fluid. *J Comp Phsyiol*. 1989;81:372-405.
25. Cochran RP, Kunzelman KS, Eddy AC, Hofer BO, Verrier ED. Modified conduit preparation creates a pseudosinus in an aortic valve–sparing procedure for aneurysm of the ascending aorta. *J Thorac Cardiovasc Surg*. 1995;109:1049-58.
26. David TE. Aoritc valve sparing operations. *Ann Thorac Surg*. 2002;73:1029-30.
27. David TE. *Commentary. J Thorac Cardiovasc Surg*. 2000;119:762-3.

**TABLE E1. Material property of the valve**

| | |
|---|---|
| Elastic modulus in the fiber direction ($E_L$) | 700 kPa |
| Elastic modulus perpendicular to the fiber direction ($E_T$) | 233 kPa |
| Poisson's ratio ($\nu_{LT}$) | 0.45 |
| Shear modulus ($G_{LT}$) | 80 kPa |

Available online at www.sciencedirect.com
ScienceDirect
Ultrasonics 48 (2008) 35–39
Ultrasonics
www.elsevier.com/locate/ultras

# Fractal dimension of 40 MHz intravascular ultrasound radio frequency signals

E. Santos Filho [a,*], Y. Saijo [a], A. Tanaka [b], T. Yambe [a], M. Yoshizawa [c]

[a] *Department of Medical Engineering and Cardiology, Institute of Development, Aging, and Cancer, Tohoku University, 4-1 Seiryomachi, Aoba-ku, Sendai 980-8575, Japan*
[b] *Faculty of Symbiotic Systems Science, Fukushima University, Japan*
[c] *Information Synergy Center, Tohoku University, Japan*

Received 18 April 2007; received in revised form 24 August 2007; accepted 24 August 2007
Available online 7 November 2007

**Abstract**

*Objective:* Fully automatic tissue characterization in intravascular ultrasound systems is still a challenge for the researchers. The present work aims to evaluate the feasibility of using the Higuchi fractal dimension of intravascular ultrasound radio frequency signals as a feature for tissue characterization.

*Methods:* Fractal dimension images are generated based on the radio frequency signals obtained using mechanically rotating 40 MHz intravascular ultrasound catheter (Atlantis SR Plus, Boston Scientific, USA) and compared with the corresponding correlation images.

*Conclusion:* An inverse relation between the fractal dimension images and the correlation images was revealed indicating that the hard or slow moving tissues in the correlation image usually have low fractal dimension and vice-versa. Thus, the present study suggests that fractal dimension images may be used as a feature for intravascular ultrasound tissue characterization and present better resolution then the correlation images.


*PACS:* 87.62; 87.59.M; 47.53.+n

*Keywords:* Intravascular ultrasound; Tissue characterization; Fractal dimension; Radio frequency signal; Coronary artery

## 1. Introduction

Intravascular ultrasound (IVUS) has been clinically applied since early 1990s. The tomographic orientation of ultrasound enables visualization of the entire circumference of the vessel wall and provide information about tissues beneath the luminal border. However, visual analysis of IVUS images by experts is usually accompanied by limitations associated with interpersonal variations, errors due to fatigue, environmental distractions, etc. Computer-aided tissue characterization of IVUS images has a potential to add objective strength to the interpretation of the expert becoming an important tool for coronary diseases diagnosis. Analysis of IVUS radio frequency (RF) signal has potential to provide powerful features for tissue characterization because it is the original source of information from the backscattered ultrasound beam.

Nair et al. [1] successfully used spectral analysis of backscattered IVUS RF signals to classify plaque composition by constructing classification trees. However, for test data, in spite of presenting accuracy of 100% for calcified-necrosis, the accuracies for fibrolipid and collagen were 83% and 69%, respectively, showing that improvements and new signal processing techniques are still necessary for a full tissue characterization in IVUS imaging.

Signal processing based on estimating fractal dimension in a time series has been successfully applied in a number of

* Corresponding author. Tel.: +81 22 717 8517; fax: +81 22 717 8518.
*E-mail address:* esmeraldo@ieee.org (E.S. Filho).

0041-624X/$ - see front matter © 2007 Elsevier B.V. All rights reserved.
doi:10.1016/j.ultras.2007.08.006

medical applications due to its capability of expressing signal irregularity [1–5].

Alacam et al. [6] showed that the features obtained by statistical modeling of RF echo can be used as decision criterion for tissue characterization in breast cancer diagnosis. They proposed the fractional differencing auto regressive moving average (FARMA) model which captures the fractal and long term correlated nature of the backscattered speckle texture. Using a linear classifier their method presented an area of 0.87 under the receiver operating characteristic (ROC) curve.

Moradi et al. [7] have presented an innovative approach for detection of prostate cancer based on the fractal analysis of RF ultrasound echo signals. They used Higuchi's [8] method to calculate the fractal dimension over a region of interest (ROI) and used it as feature to detect the prostate cancer through a Bayesian classifier [9]. Their algorithm presented accuracy of 86% indicating the feasibility of their approach.

Saijo et al. [10,11], have developed a method for tissue characterization based on two-dimensional correlation between two consecutive frames of an IVUS sequence. This technique was shown capable of distinguishing regions of fast moving fluid like blood or surrounding tissue from region of slow moving or stable like the vessel wall.

In this work, we investigate the feasibility of using the Higuchi's fractal dimension as a feature for tissue characterization in IVUS through comparison with correlation images.

## 2. Materials and methods

IVUS data were acquired with an IVUS console Clear View Ultra (Boston Scientific Inc., Natick-MA, USA) and 40 MHz mechanically rotating IVUS catheter Atlantis SR Plus (Boston Scientific Inc., Natick-MA, USA) and the pulse repetition rate was 7680 Hz. RF data were digitized and stored in a personal computer (PC) (Dell 8250, Pentium 4, 2.4 GHz, 1.50 GB RAM, Dell Inc., Round Rock, TX, USA) using an A/D board GAGE Compuscope 8500 (500 Msamples/s, with 8 bits of resolution, Gage Applied Inc., Montreal, Quebec, Canada) for off-line analysis. The algorithms were developed using MATLAB (The Mathworks Inc., Natick, MA, USA). A single frame of the IVUS system consisted of 256 lines so that 7680 pulses made 30 frames per second (f/s). RF signal data were acquired in vivo from 14 human left anterior descending (LAD) coronary arteries during percutaneous transluminal coronary angioplasty (PTCA). The patients average age was $72 \pm 12$ years and six of them presented detected calcification regions and one detected soft plaque in their IVUS images. This process was approved by a local investigation review board and was performed in accordance with the ethical principles for medical research involving human subjects. We obtained written informed consent from all the subjects.

### 2.1. Fractal dimension image

The concept of fractal dimension is based on the property of self-similarity. In spite of not being self-similar over all the scales, the IVUS RF signals usually present some level of self-similarity within some range and thus the Higuchi fractal dimension can be used as an efficient method to express the irregularity of the RF signals in the ROIs of appropriate size.

Higuchi's algorithm [8] is proven to be a stable method to estimate the fractal dimension of a time series and, more importantly, works well for time series with few samples. The algorithm, computes mean length of the signal at different scales, plots a log–log graph of length versus scale and measures the slope of the linear fit of this graph as the fractal dimension.

Thus, for generation of the fractal dimension images the following algorithm was used.

**Algorithm.** For each ROI defined by the position of a 100 points wide sliding window, the following steps were used:

1. Extract the signal envelop through the calculation of the absolute value of the Hilbert transform.
2. Normalize the envelop by dividing it by its maximum value in that sample.
3. Calculate the fractal dimension of the normalized signal using the Higuchi method.
4. The sliding window is shifted of 25 points and the above steps are repeated for all RF lines that comprise the IVUS image.

### 2.2. Correlation image

Conventional B-mode IVUS images were generated from RF signals by software developed by our group [10]. Then the IVUS image was divided into $64 \times 64$ square shape ROIs. Template matching method was applied for calculation of correlation and displacement of the ROIs between the consecutive two frames. Template matching is the process of determining the presence and the location of a reference image or an object inside a scene image under analysis by a spatial cross-correlation process. Fig. 1 shows the schematic illustration of template matching method. If the coordinates of the center of the ROI in the first frame (a) are defined as $p(0,0)$ and the most similar patterned ROI in the next frame (b) is $q(k,l)$, the correlation is given by:

$$R_{fg}(k,l) = \frac{\sum_{i=0}^{n^2-1}(f_i - \bar{f}_i)(g_i - \bar{g}_i)}{\sqrt{\sum_{i=0}^{n^2-1}(f_i - \bar{f}_i)^2 \sum_{i=0}^{n^2-1}(g_i - \bar{g}_i)^2}} \quad (1)$$

where $f_i$ and $g_i$ are pixels inside the ROI in consecutive frames, $\bar{f}_i$ and $\bar{g}_i$ are the corresponding mean gray level values of each ROI, and $n$ is the length of the side of the square shaped ROI.

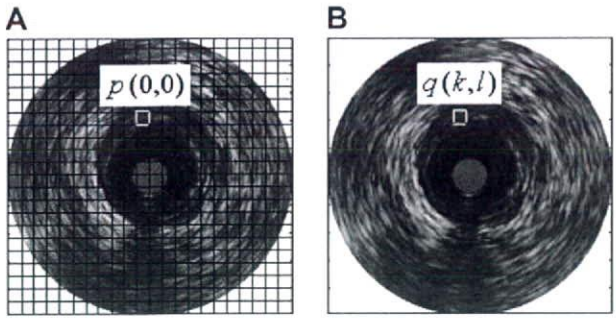


Fig. 1. Schematic illustration of template matching method. The coordinates of the center of the ROI in the first frame (A) is defined as $p(0, 0)$ and the most similar ROI in the next frame (B) is $q(k, l)$.

Based on our tests, we could observe that the moving regions such as blood and surrounding tissues presented correlation values below 0.5 and the regions of vessel wall presented correlation values above 0.75. The vessel wall was assumed stable during 1/30 s.

## 3. Results

In Fig. 2, we can see an example of two samples of IVUS RF signal extracted from the region of blood and the region of vessel wall. It can be seen that the sample extracted from the blood region presents a more irregular shape than the sample from the region of vessel. As the fractal dimension can be regarded as a measure of irregularity, we used the fractal dimension as a feature for tissue characterization.

In Fig. 3C and F, we can see two examples of fractal dimension images. They are images whose pixel colors represent the fractal dimension of a 100 points wide sliding window centered at the corresponding position in the RF line. In spite of being quite noisy, we can observe that the regions of lumen present fractal dimension values higher (light blue and green) than the vessel wall region (dark blue). More homogeneous regions, like calcification regions for example, present a lower fractal dimension value (dark blue).

Also, in Fig. 3B and E, we can compare the fractal images with the correlation images, which are images whose pixel value represents the correlation index calculated through Eq. (1). The correlation image shows its lowest level in the regions of blood (light blue), which is the most dynamic region. This fact is also detected through the fractal dimension image.

In Fig. 3A, we can observe clearly the boundary lumen/vessel that is confirmed in Fig. 3B, where the lumen region presents correlation values usually below 0.5, represented by light green or light blue, due to the fast moving blood. The red region is the static or slow moving vessel wall. In the fractal dimension image (Fig. 3C) we can observe that

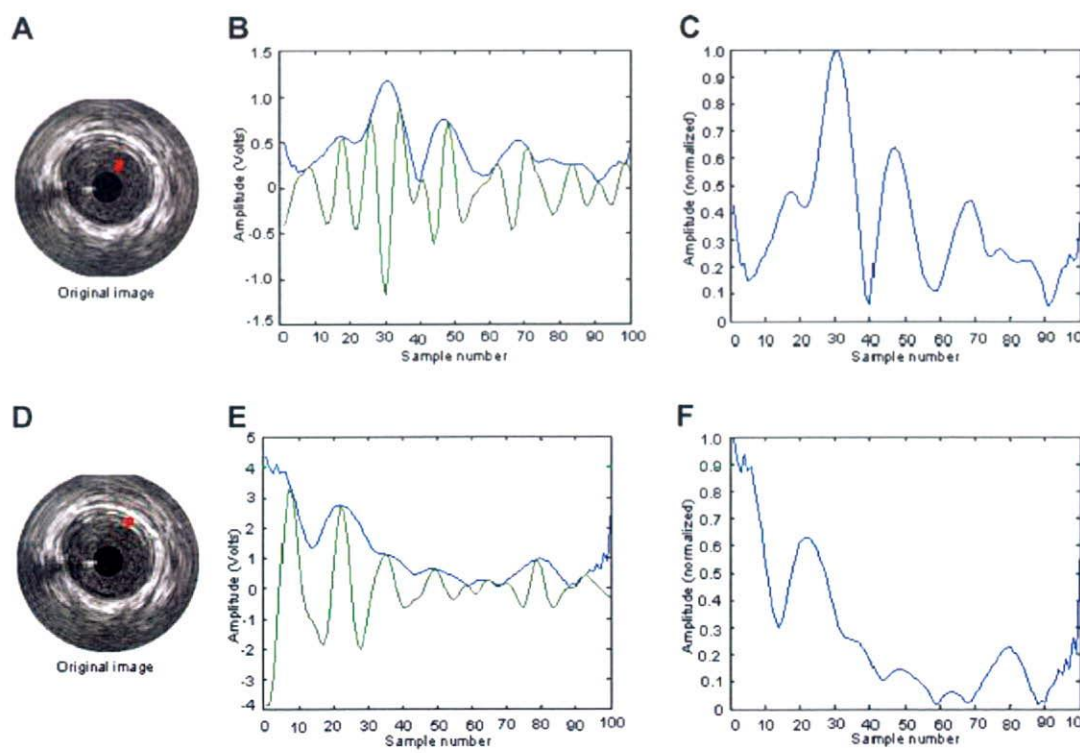


Fig. 2. Example of RF signal ROIs extracted from lumen region (A) and vessel wall region (D). The small regions in red in (A) and (D) indicate the position from where the ROIs were extracted. They are 100 samples length ROIs. (B) and (E) are the graphs of the RF signals ROIs (in green) and their respective envelop (in blue). (C) and (F) are graphs of the normalized envelops.

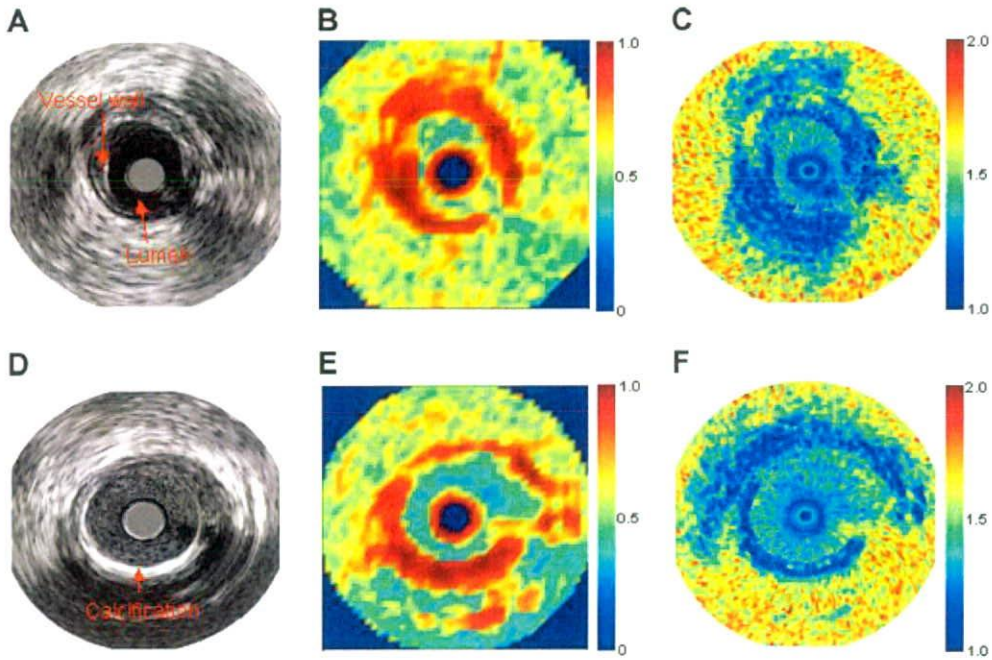


Fig. 3. Comparison between correlation image and fractal dimension image. (A) and (D) are the original images. (B) and (E) are examples of correlation images. (C) and (F) are example of fractal dimension images.

the lumen region is light blue whereas the vessel wall region is dark blue. This means that the fractal dimension in the lumen region, usually between 1.25 and 1.5, is higher than the fractal dimension in the vessel wall region that is usually below 1.20. This suggests that the irregularity level of the RF signal expressed by Higuchi fractal dimension can be used, to some extent, to characterize the moving tissues. The region outside the vessel in Fig. 3C is quite yellow and red, with fractal dimension values around 1.7, mainly because this is a region of high noise level. The corresponding area in Fig. 3B present low correlation level indicating fast moving connecting tissues. Additionally, we can observe in Fig. 3E and F that the region of calcium is also a region of high correlation value and low fractal dimension. It can also be observed that the fractal dimension images present better resolution than the correlation images.

## 4. Discussion

The examples in Fig. 2 showed that, besides the differences in amplitude, the irregularity of the envelop is fairly different in these both regions suggesting that a measure of signal irregularity could be a useful discriminator for regions of vessel wall and lumen. Saijo et al. [10] have observed similar results through the two-dimensional correlation analysis. Their results were validated by comparisons with histology data.

Accordingly to our tests, RF signal samples shorter then 60 points did not provide acceptable results because the images generated using a window of this width did not present clear contrast between the lumen and the vessel wall. The highest contrast is achieved for sliding window with width of around 100 points. Sliding windows wider than 100 points did not present visible improvements.

As reported in [8], the Higuchi method presented more stable results when compared with other methods based on power spectrum. In tests performed with IVUS RF signals the power spectrum based fractal dimension did not provide satisfactory results, probably, due to the large amount of noise, suggesting the robustness of Higuchi method.

Using the PC described in Section 2, the average processing time needed to generate the fractal dimension images was 128 s. This suggests that the proposed algorithm may be used in real time if more powerful hardware is used and the program is optimized.

The fractal dimension images presented an average contrast-to-noise ratio (CNR) of 3.73 whereas the correlation image presented 3.05. However, together with lower CNR, the correlation images present lower resolution. Thus the fractal images with a CNR of 3.05 seen to present a satisfactory trade-off between noise and resolution because the resultant fractal dimension images presented less distortion of the lumen contour than the correlation images as can be seen in Fig. 3.

Comparing images from different patients, for example, patients with calcification and patients without calcification, we could observe that the fractal dimension values in the calcification regions is similar to levels presented in the vessel wall region, as shown in Fig. 3. This

suggests that the fractal dimension images may not be useful in calcification detection. In tests with image containing soft plaque, the resulting fractal dimension image did not present clear contrast between the soft plaque and blood. Thus, this method does not seem likely to be a good discriminator for plaques. However, it may be useful as a pre-processing stage toward luminal contour detection.

## 5. Conclusion

A comparison between correlation images and fractal dimension images was presented and we could observe that, in general, the regions of high correlation values in the correlation image correspond to the regions of low fractal dimension in the corresponding fractal dimension image and vice-versa. This fact suggests that the fractal dimension, as measure of irregularity of the RF echo signal, can be also an indicator of the moving characteristic of the interrogated tissue as well as the correlation image. However, the fractal dimension image has the advantage of presenting more clearly the fine details of the luminal contour when compared to the correlation images.

## Acknowledgement

This study was supported by the Grants-in-Aid from the Ministry of Health, Labor and Welfare of Japan (H17-nano-001).

## References

[1] A. Nair, B.D. Kuban, N. Obuchowski, D.G. Vince, Assessing spectral algorithms to predict atherosclerotic plaque composition with normalized and raw intravascular ultrasound data, Ultrasound in Medicine and Biology 27 (2001) 1319–1331.
[2] R. Jennane, W.J. Ohley, S. Majumdar, G. Lemineur, Fractal analysis of bone X-ray tomographic microscopy projections, IEEE Transactions on Medical Imaging 20 (2001) 443–449.
[3] T. Stosic, B.D. Stosic, Multifractal analysis of human retinal vessels, IEEE Transactions on Medical Imaging 25 (2006) 1101–1107.
[4] P. Asvestas, S. Golemati, G.K. Matsopoulos, K.S. Nikita, A.N. Nicolaides, Fractal dimension estimation of carotid atherosclerotic plaques from b-mode ultrasound: a pilot study, Ultrasound in Medicine and Biology 28 (2002) 1129–1136.
[5] W.L. Lee, Y.C. Chen, K.S. Hsieh, Ultrasonic liver tissues classification by fractal feature vector based on m-band wavelet transform, IEEE Transaction on Medical Imaging 22 (2003) 382–392.
[6] B. Alacam, B. Yazici, N. Bilgutay, F. Forsberg, C. Piccoli, Breast tissue characterization using modeling of ultrasonic RF echo, Ultrasound in Medicine and Biology 30 (2004) 1397–1407.
[7] M. Moradi, P. Ablmaesumi, P.A. Isolato, D.R. Siemens, E.E. Sauerbrei, P. Mousavi. A new feature for detection of prostate cancer based in RF ultrasound echo signals, in: Proceedings of IEEE Ultrasonics Symposium, 2006. pp. 2084–2087.
[8] T. Higuchi, Approach to an irregular time series on the basis of the fractal theory, Physica D 31 (1988) 277–283.
[9] R.M. Rangayyan, Biomedical Image Analysis, CRC Press, Boca Raton, FL, USA, 2005, pp. 1118.
[10] Y. Saijo, A. Tanaka, T. Iwamoto, E. Santos Filho, M. Yoshizawa, A. Hirosaka, M. Kijima, Y. Akino, Y. Hanadate, T. Yambe, Intravascular two-dimensional tissue strain imaging, Ultrasonics 44 (2006) e147–e151.
[11] Y. Saijo, A. Tanaka, N. Owada, Y. Akino, S. Nitta, Tissue velocity imaging of coronary artery by rotating-type intravascular ultrasound, Ultrasonics 42 (2004) 753–757.

Available online at www.sciencedirect.com
ScienceDirect
Displays 29 (2008) 167–175
DISPLAYS
www.elsevier.com/locate/displa

# Quantitative evaluation of effects of visually-induced motion sickness based on causal coherence functions between blood pressure and heart rate

N. Sugita [a,*], M. Yoshizawa [b], A. Tanaka [c], K. Abe [d], S. Chiba [e], T. Yambe [f], S. Nitta [f]

[a] Graduate School of Engineering, Tohoku University, 6-6-05 Aoba, Aramaki, Aoba-ku, Sendai 980-8579, Japan
[b] Information Synergy Center, Tohoku University, 6-6-05 Aoba, Aramaki, Aoba-ku, Sendai 980-8579, Japan
[c] Faculty of Symbiotic Systems Science, Fukushima University, 1 Kanayagawa, Fukushima 960-1296, Japan
[d] College of Engineering, Nihon University, 1 Tamuramachi Tokusada, Nakakawahara, Koriyama 963-8642, Japan
[e] Sharp Corporation, 1-9-2 Nakase, Mihama-ku, Chiba 261-8520, Japan
[f] Institute of Development, Aging and Cancer, Tohoku University, 4-1 Seiryo-machi, Aoba-ku, Sendai 980-8575, Japan

Available online 18 October 2007

**Abstract**

Recent advances in video and computer graphics technologies have been accelerating creation of novel visual images including complex and intensive motion of the visual point. However, there are concerns about adverse effects of these images on humans such as visually-induced motion sickness (VIMS). To evaluate the effects of VIMS, the present study has analyzed the linearity of the baroreflex system and that of the mechanical hemodynamic system by using causal coherence functions. The causal coherence functions have a capability of calculating linear correlation between two systems independently even if the systems are connected with each other to compose a closed-loop system. In the experiment, healthy human subjects' heart rate and continuous blood pressure were measured to obtain the causal coherence functions when the subjects were watching an unstable video image. The results showed that there were significant differences in the causal coherence functions as well as the traditional coherence function between the sick and the well groups and that the hemodynamic system was mainly disturbed by VIMS rather than the baroreflex system. These findings suggest that the causal coherence functions of the two systems and the traditional coherence function of the whole system gave different information from one another. This fact implies that the causal coherence functions will be useful and objective means to quantify VIMS as functions of time.


*Keywords:* Blood pressure; Heart rate; Visually-induced motion sickness; Causal coherence function

## 1. Introduction

Recent rapid development in display technologies has exposed many people to new display environments such as widescreen TV sets with high resolution and deep contrast, artificial three-dimensional displays, and head mounted displays used in virtual reality or video games. In addition, progress of video and computer graphics technologies is accelerating creation of innovative images including complex and intensive motion of the visual point which traditional camera techniques cannot realize physically.

However, there are concerns about adverse effects of visual stimulation on humans. At a junior high school in Japan on July 10, 2003, there was the incident in which 36 students out of 294 were treated in a hospital because they had complained of dizziness and nausea in watching a video image taken by an amateur cameraman with a swaying handy camera [25]. This is a typical case of visually-induced motion sickness (VIMS). The novel display environments mentioned above tends to cause VIMS.

For reduction of the risk of VIMS, it is important to find the condition for causing VIMS. To do this, it is necessary to evaluate how seriously a subject suffers from VIMS.

* Corresponding author. Tel.: +81 227957130; fax: +81 222639163.
*E-mail address:* sugita@yoshizawa.ecei.tohoku.ac.jp (N. Sugita).

0141-9382/$ - see front matter © 2007 Elsevier B.V. All rights reserved.
doi:10.1016/j.displa.2007.09.017

One of the most effective but subjective methods for evaluating VIMS is the simulator sickness questionnaire (SSQ) proposed by Kennedy et al. [12]. Many studies using the SSQ have shown that the score based on the SSQ is a useful index for evaluating the level of VIMS. In general, however, the results obtained from subjective methods such as the SSQ are affected by viewers' psychological bias and preference for the image so much that there are great differences in the results among individuals. Moreover, it is unlikely to build an automatic system that can predict a certain subject's sign of VIMS on the basis of some questionnaires because it is difficult to obtain subjective indices in a real-time fashion.

On the other hand, there is little objective method based on noninvasive measurements for evaluating VIMS. Postural stability is frequently used as one of objective indices for evaluating motion sickness [5,20–22]. However, postural stability is closely related to vection or disorientation [17] but cannot directly represent physiological symptoms such as headache, eyestrain, and nausea.

In this situation, other objective and physiological methods for evaluating VIMS are desired. The purpose of this study is to find an objective and quantitative index representing the effect of VIMS in terms of the autonomic nervous activities.

There are many indices for analysis of the autonomic nervous activities based on noninvasive physiological measurements such as heart rate and blood pressure variabilities [18,16]. However, these indices are not always useful for our attempt due to large inter-individual difference and low reproducibility.

In the previous work, the authors focused on the correlation between heart rate and blood pressure variability, that is to say, baroreflex function. In this work, we have reported that the maximum cross-correlation coefficient between heart rate and blood pressure strongly reflects the change in the autonomic nervous activity caused by exposure of visual stimulation [27,23]. In the case of a man who does not receive any stimulation, his heart rate changes in response to blood pressure through the autonomic nervous system, and then the correlation between these parameters is somewhat fixed. On the other hand, if he watches a video image and feels VIMS, it seems that physiological and/or psychological effects interfere in the relation, or the effects change the activity of the autonomic nervous system, then the correlation decreases.

However, the index we proposed cannot consider the causality of the baroreflex system. To understand the mechanism of the biological effect of visual stimulation more in detail, we should analyze both the baroreflex and the mechanical paths independently, these paths form a baroreflex closed-loop, and know which path is more affected by the biological reaction to the stimulation.

In this study, causal coherence functions [19] were introduced to analyze the effect of VIMS. The causal coherence functions have a capability of calculating linear correlation between two systems independently even if the systems are connected with each other to compose a closed-loop such as the baroreflex system. In the experiment, healthy human subjects' heart rate and continuous blood pressure were measured to obtain the causal coherence functions when the subjects were watching an unstable video image taken by a swaying handy camera.

## 2. Methods

### 2.1. Experiment

Fig. 1 shows the schematic illustration of the experiment carried out in this study.

In the experiment, a video image clipped from the film "The Blair Witch Project" [8] was used as a visual stimulation shown to human subjects. The film is notorious for inducing VIMS because this was taken by a handheld camera swayed intentionally to enhance reality in spite of a fiction. Most of scenes in the film were shot in a town or the woods and violent scenes were cut out to prevent the emotional effect. The video image was projected from back side of a screen by a DLP projector (resolution: $1024 \times 768$, brightness: 800ANSI lumens).

The total number of test subjects was 56 (34 males and 22 females; aged 18–35; mean age: 22.8). Informed consent was obtained from all the subjects before the experiment. Each subject was told to watch a series of images as follows: (1) a 3 min-long still picture of a landscape for control; (2) the 15 min-long the swaying video image explained above; (3) the same 3 min-long still picture as (1). Before the trial, the subject answered a questionnaire about his or her physical and mental state. After the trial, the SSQ [12] was charged to the same subject. The SSQ contains 16 items to check the subject's physical disorder. The subject rated the degree of these items in 4 levels. Three subscales, i.e., nausea, oculomotor, and disorientation, were calculated on the basis of these items, and a total score was calculated with these subscales.

During the trial, ECG and continuous blood pressure were measured by an ECG amplifier and a finger-tip-type blood pressure sensor (PORTAPRES; Finapres Inc.), respectively. These signals were converted to digital signals by a 16-bit A/D converter (MP100; BIOPAC Systems Inc.) and stored in a personal computer every 1 ms. Heart rate (HR [$\mathrm{min}^{-1}$]) was calculated from the reciprocal of the inter-R-wave interval of the ECG signal. Systolic blood pressure (SBP [mmHg]) was obtained as the maximum value of the blood pressure signal over one heartbeat.

### 2.2. Analysis

In this study, not only the coherence function ($K^2(f)$; $f$: frequency in Hz) but also two causal coherence functions ($K^2_{\mathrm{SBP}\to\mathrm{HR}}(f)$ and $K^2_{\mathrm{HR}\to\mathrm{SBP}}(f)$) were calculated according to the following procedure. This calculation is based on the bivariate autoregressive (AR) model of the cardiovascular system shown in Fig. 2 proposed by Porta et al. [19].

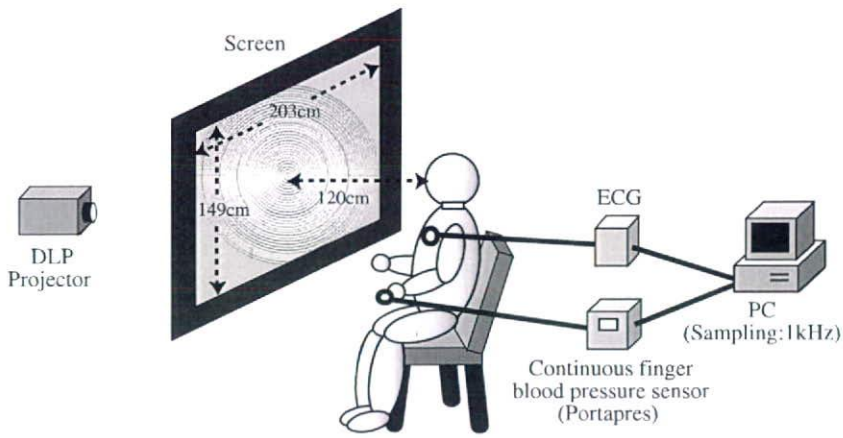


Fig. 1. Schematic illustration of the experiment.

First, the beat-to-beat variables HR and SBP are interpolated by the cubic spline function and re-sampled every $\Delta t = 0.5$ s to yield time discrete variables HR($k$) and SBP($k$); $k = 1, 2, 3, \ldots$, respectively.

Let $y_1(k)$ and $y_2(k)$ denote HR($k$) and SBP($k$), respectively. Using a function *arx* for system identification included in a scientific and engineering calculation language *Matlab* (Mathworks Inc.), the polynomial elements ($A_{11}(z)$, $A_{22}(z)$, $A_{12}(z)$, and $A_{21}(z)$) with the forward operator $z$ of the bivariate AR model shown in Fig. 2 are calculated under the assumption that the noise source ($w_i(k); i = 1, 2$) is a white Gaussian noise with zero mean and the variance of $\lambda_i$.

Then the power spectra ($S_{11}(f)$ and $S_{22}(f)$) of $y_1(k) = \mathrm{HR}(k)$ and $y_2(k) = \mathrm{SBP}(k)$ are given by

$$S_{11}(f) = |\Delta(z)|^2 \cdot \left[ |1 - A_{22}(z)|^2 \cdot \lambda_1^2 + |A_{12}(z)|^2 \cdot \lambda_2^2 \right] \Big|_{z=e^{j2\pi f \Delta t}} \quad (1)$$

$$S_{22}(f) = |\Delta(z)|^2 \cdot \left[ |A_{21}(z)|^2 \cdot \lambda_1^2 + |1 - A_{11}(z)|^2 \cdot \lambda_2^2 \right] \Big|_{z=e^{j2\pi f \Delta t}} \quad (2)$$

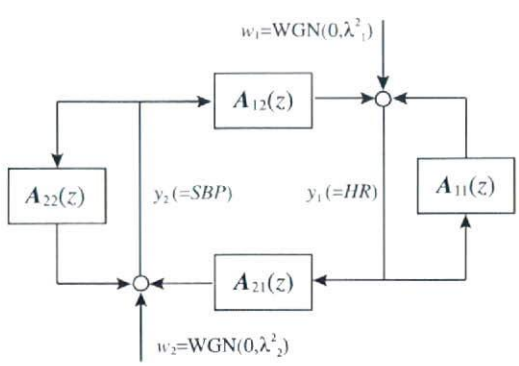


Fig. 2. Closed-loop bivariate autoregressive model for the cardiovascular system. WGN($0, \lambda_i^2; i = 1, 2$) shows white Gaussian noise with zero mean and variance of $\lambda_i^2$.

The cross-spectrum ($S_{12}(f)$) from SBP($k$) to HR($k$) is given by

$$S_{12}(f) = |\Delta(z)|^2 \cdot \left[ \{1 - A_{22}(z)\} \cdot A_{21}(z^{-1}) \cdot \lambda_1^2 + A_{12}(z) \cdot \{1 - A_{11}(z^{-1})\} \lambda_2^2 \right] \Big|_{z=e^{j2\pi f \Delta t}} \quad (3)$$

where

$$\Delta(z) = \left[ \{1 - A_{11}(z)\} \cdot \{1 - A_{22}(z)\} - A_{12}(z) \cdot A_{21}(z) \right]^{-1} \quad (4)$$

The squared coherence function $K^2(f)$ between HR($k$) and SBP($k$) is defined as

$$K^2(f) = \frac{|S_{12}(f)|^2}{S_{11}(f) \cdot S_{22}(f)} \quad (5)$$

The index $K^2(f)$ represents the whole linearity of the system shown in Fig. 2. Here, if one of the AR parameters representing the strength of the causal coupling is set to zero virtually, the linearity of the each arm in the closed-loop is defined as

$$K^2_{\mathrm{SBP}\to\mathrm{HR}}(f) = K^2(f)\big|_{A_{21}(z)=0} \quad (6)$$

$$K^2_{\mathrm{HR}\to\mathrm{SBP}}(f) = K^2(f)\big|_{A_{12}(z)=0} \quad (7)$$

$K^2_{\mathrm{SBP}\to\mathrm{HR}}(f)$ and $K^2_{\mathrm{HR}\to\mathrm{SBP}}(f)$ are causal coherence functions and correspond to the neural baroreflex system and the mechanical hemodynamics in the cardiovascular system, respectively.

The dimension of the model was selected using Akaike's Information Criterion [1]. Two steps (1 s) delay was inserted in HR($k$) because the $k$th HR cannot immediately affect the $k$th SBP [2].

The mean values of $K^2(f)$, $K^2_{\mathrm{SBP}\to\mathrm{HR}}(f)$ and $K^2_{\mathrm{HR}\to\mathrm{SBP}}(f)$ over the low frequency band ($0.05\ \mathrm{Hz} < f < 0.15\ \mathrm{Hz}$) and those over the high frequency band ($0.15\ \mathrm{Hz} < f < 0.45\ \mathrm{Hz}$) were calculated time-discretely every 10 s on the basis of the last 2 min-long data. The low frequency band corresponds to the so-called Mayer wave which is closely related to the baroreflex modulated by both sympathetic and parasympathetic nervous activities [7]. On the other hand, the high frequency band corresponds to the respiratory sinus